Progress toward atomic diagnostics of ultrahigh laser intensities

M. F. Ciappina,[1] S. V. Popruzhenko,[2,3] S. V. Bulanov,[1] T. Ditmire,[4] G. Korn,[1] and S. Weber[1]
[1]*Institute of Physics of the ASCR, ELI-Beamlines project, Na Slovance 2, 182 21 Prague, Czech Republic*
[2]*Max Planck Institute for the Physics of Complex Systems, 01187 Dresden, Germany*
[3]*Prokhorov General Physics Institute of the Russian Academy of Sciences, 119991 Moscow, Russia*
[4]*Center for High Energy Density Science, C1510, Department of Physics, University of Texas at Austin, Austin, Texas 78712, USA*

(Received 18 January 2019; published 5 April 2019)

We discuss and numerically test a method for direct and unambiguous measurement of ultrahigh laser intensities exceeding 10^{20} W/cm^2. The method is based on the use of multiple sequential tunneling ionization of heavy atoms with sufficiently high ionization potentials. We show that, due to a highly nonlinear dependence of tunneling ionization rates on the electromagnetic field strength, an offset in the charge distribution of ions appears sufficiently sensitive to the peak value of intensity in the laser focus. A simple analytic theory is presented which helps in estimating the maximal charge state produced at a given intensity via the tunnel-ionization mechanism. The theory also allows for calculating qualitatively a distribution in charge states generated in different parts of the laser focus. These qualitative predictions are supported by numerical simulations of the tunneling cascades developed in the interaction of a short intense laser pulse with a low-density target consisting of noble gases including argon, krypton, and xenon. Results of these simulations show that, using this technique, intensities in the range 10^{20}–10^{24} W/cm^2 can be measured with sufficient reliability. The method could be extremely useful and of high demand in view of the expected commissioning of several new laser facilities capable of delivering ultrapowerful light pulses in this domain of intensities.

DOI: 10.1103/PhysRevA.99.043405

I. INTRODUCTION

During the past few decades, the continuous development of high-power laser sources operating at optical and infrared wavelengths has lead to a considerable growth in intensities of electromagnetic radiation available in laboratories. Presently, intensities up to 10^{19} W/cm^2 are being routinely used in many laser facilities, and several lasers of petawatt (PW) power [1] deliver pulses of intensity up to 10^{21} W/cm^2. Singular reports of even higher intensities $\simeq 10^{22}$ W/cm^2 [2–4] are still lacking independent and unambiguous evidences. However, the forthcoming commissioning of several new 10 PW class laser facilities [5–10] opens a way to a considerable step forward. For a laser power of 3 PW, expected to be reached at the ELI-Beamlines facility within the next 2–3 years, the peak intensity in a 3λ focal spot of an 800 nm laser pulse will exceed 5×10^{22} W/cm^2. With 10 PW laser pulses focused down to the diffraction limit, intensities on the order of $\simeq 10^{24}$ W/cm^2 or even higher can be achieved.

This breakthrough is expected to make new regimes of laser-matter interactions accessible for experimental research including the radiation-dominated regime, where radiation friction forces play the major role in plasma dynamics, observation of relativistic tunneling, generation of QED cascades of elementary particles developed from seed particles in a laser focus, and many other effects inaccessible at presently available laser intensities. For the overview of this newly emerging research area we direct the reader to reviews [11–13] and the literature quoted there.

In view of these expectations, the problem of precise and unambiguous determination of the electromagnetic field intensity in a laser focus becomes of exceptional importance. Here we suggest using tunneling ionization of multicharged ions as a probe of laser intensity. The main advantage of this method has its root in the highly nonlinear dependence of the tunneling ionization probability on the electromagnetic field strength, so that a relatively small variation in intensity leads to orders of magnitude change in the ionization rate. Consequently, the maximal ionic charge observed in a laser focus becomes a highly sensitive function of the peak intensity. The shape of photoelectron spectra and positions of the spectral maximum in a circularly polarized field [14] and of the high-energy cutoff in a linearly polarized field [15] are also sensitive to the value of intensity and have been used for its determination. Generally, at moderate intensities $\mathcal{I} \leqslant 10^{15}$ W/cm^2, when single-electron ionization remains the dominant process, and effects of ponderomotive scattering play no significant role in laser pulses of femtosecond duration, photoelectron spectra are the most efficient measure of intensity [16,17]. With its value growing, multiple ionization comes into play along two competing mechanisms known as sequential and nonsequential ionization, with the latter triggered by recollisions [18–21]. Interplay of the two mechanisms makes the interval $\mathcal{I} \simeq 10^{15}$–$10^{17}$ W/cm^2 difficult for univocal determination of intensity via the ionization process. A further increase of intensity simplifies the situation again. As soon as the electron motion after the ionization step becomes relativistic, which for $\lambda = 800$ nm happens at $\mathcal{I} \approx 10^{17}$ W/cm^2, the longitudinal photoelectron drift induced by the Lorentz force suppresses recollisions, so that the sequential tunnel ionization remains the only relevant mechanism.

Simultaneously, deeper electronic shells are stripped out by the laser: helium is fully ionized at $\mathcal{I} \approx 5 \times 10^{16}$ W/cm^2 and neon at $\mathcal{I} \approx 10^{20}$ W/cm^2. Thus probing higher intensities with ionization requires a target consisting of high-Z atoms [22,23].

A large number of experimental works considered multiple ionization of atoms by intense optical and infrared laser radiation. As far as ultrahigh intensities are concerned, Walker *et al.* [24,25] and Yamakawa *et al.* [26,27] studied ionization of noble gases at intensities up to 10^{19} W/cm^2 aiming at rather the opposite purpose, namely, to check validity of the tunneling ionization theory assuming the value of intensity known. Although in their calculations they did not consider effects of the intensity distribution over the laser focus and simply estimated the maximal ionic charge number using the tunneling rate formulas [28–32], a fairly good agreement with the data was demonstrated.

In this contribution, we suggest using the setup of [24–27] in the opposite way: the unknown value of the peak intensity and, to some extent, of the spatial intensity distribution in the focus can be reconstructed from the distributions of ionic charge states. This idea has been rather widely spread in the strong field community (see, e.g., Refs. [22,23]) with, however, little emphasis on both the experimental constraints needed for its realization and on the accuracy which can be achieved within this approach. Additionally, to the best of our knowledge, a systematic and exhaustive theoretical study of this method, joint with its limitations, is still missing.

To verify the validity of this idea, we employ the theory of sequential tunneling ionization and numerically calculate the charge spectra by varying the laser peak value. Our paper is organized in the following way. Section II presents qualitative estimates justifying the theory of single-particle nonrelativistic sequential tunneling which applies for the considered problem up to intensities of $\mathcal{I} \approx 10^{24}$ W/cm^2. Here also a brief summary of the tunneling ionization theory is given, in the part which relates to the total ionization rates. Using analytic formulas for the rate of tunneling ionization, a simple estimate for the offset ionization potential corresponding to the highest charge state present in the spectrum is given. A system of rate equations based on the ionization rates is formulated for the case of ionization of argon, krypton, and xenon. Essential simplifications of the full system, making it accessible for fast numerical computation, are introduced and discussed here. Results of numerical calculations are presented as well and compared to the theoretical predictions of Sec. III. The last section contains a brief conclusion. A complete description of the systems of rate equations as well as all the parameters needed for their numerical implementation are given in the Appendices. Atomic units $e = m_e = \hbar = 1$ with the speed of light $c = 1/\alpha$, where α is the fine-structure constant, are used unless stated otherwise.

II. THEORY

A. Qualitative considerations

Our theoretical approach is based on the following physical picture.

(1) A gas in the laser focus is kept at sufficiently low pressure, so that neither nonlinear propagation and plasma effects in the medium nor electron-ion collisions play any significant role. At a concentration of atoms $n_0 = 10^{14}$ cm^{-3} and an average ionic charge $\bar{z} = 20$ the plasma frequency is of the order of $\omega_p \simeq 10^{12}$ s^{-1}, so that no plasma oscillations take place during the interaction with a laser pulse of a 100 fs or shorter duration. Photoelectron energies ε_e in a laser field are of the order of the ponderomotive energy, so that in the ultrarelativistic case we are interested in results

$$\varepsilon_e \approx \sqrt{1 + \frac{a_0^2(1+\rho^2)}{2}}c^2 \simeq a_0 c^2, \tag{1}$$

where a_0 is the dimensionless field amplitude defined as

$$a_0 = \frac{E_0}{\omega c}, \tag{2}$$

with E_0 and ω being the laser field amplitude and frequency, respectively, and ρ being the laser field ellipticity ($\rho = 0$ for linear and $\rho = \pm 1$ for circular polarization). Equation (1) gives energies $\varepsilon_e \approx 4 \times 10^6$ eV and $\varepsilon_e \approx 4 \times 10^8$ eV for $\mathcal{I} = 10^{20}$ W/cm^2 and $\mathcal{I} = 10^{24}$ W/cm^2, respectively. At such energies, cross sections of elastic and inelastic electron-ion collisions are comparable to that of bremsstrahlung, with none of them exceeding 10^{-20} cm^2, even at the lower boundary of the intensity interval (for numerical values and formulas see, e.g., Refs. [33,34]). As a result, the mean free path of electrons exceeds the focal size (which is limited by several microns for the tight focusing necessary to reach the highest values of intensity) by several orders in magnitude. At the same time, the number of atoms in the interaction volume, estimated assuming the diffraction-limit focusing $N_a \simeq n_0\lambda^3 \approx 10^2$, remains sufficiently high to reliably record the distribution in charge states with a typical time of flight (TOF) ion detector.

(2) We assume multiple ionization to be sequential, so that electrons leave an atom independently, one after another. This assumption can be justied by noting that the time of flight of the electron under the potential barrier

$$\tau_{\rm sb} \simeq \frac{b}{v_0} \approx \frac{\sqrt{I_p}}{\sqrt{2}E_0}, \tag{3a}$$

where $b = I_p/E_0$ is the barrier width and $v_0 = \sqrt{2I_p}$ is the characteristic electron velocity in a bound state with ionization potential $I_{\rm p}$, is much longer than the characteristic time of the electron motion in the same bound state

$$\tau_{\rm corr} \simeq \frac{a_B}{v_0} \approx \frac{1}{2I_p}. \tag{3b}$$

Here $a_B \simeq 1/\sqrt{2I_p}$ is the characteristic size of the bound state (Bohr radius). The ratio of these two times is

$$\frac{\tau_{\rm corr}}{\tau_{\rm sb}} \simeq \frac{E_0}{E_{\rm ch}} \equiv F, \quad E_{\rm ch} = (2I_p)^{3/2}, \tag{3c}$$

where $E_{\rm ch}$ is the characteristic electric-field strength at the Bohr orbit of the bound state and F is known as the reduced field [31]. For tunneling or multiphoton ionization the reduced field is always numerically small, $F \ll 1$, and its typical value decreases with increase of both the ionization potential and laser intensity, as we will demonstrate below.

(3) Although the electron motion after the ionization event quickly becomes ultrarelativistic, the tunneling itself proceeds

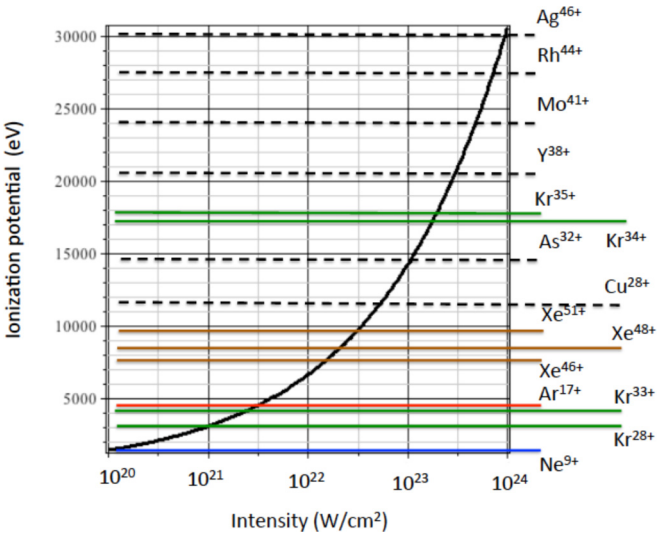

FIG. 1. Ionization offset, Eq. (14), shown by a thick black line as a function of laser intensity. Ionization potentials of several highly charged ions are shown by horizontal lines, including neon (blue), argon (red), krypton (green), and xenon (brown). Ionization potentials of Xe^{52+} and Xe^{53+} exceed 40 keV and lay above the selected energy range. The plot allows estimating the charge numbers whose distribution should be calculated numerically in order to calibrate the intensity within some certain interval. If only noble gases are used, two gaps in the laser energy determination appear, i.e., there exists a range in the laser intensity that cannot be covered using only these atomic species. The respective intervals of intensity are $\mathcal{I} \approx 3\times10^{22}$–$2\times10^{23}$ W/cm^2 and $\mathcal{I} > 2.5\times10^{23}$ W/cm^2. These gaps can be filled using other elements than noble gases. Dashed lines show ionization potentials of several metals with only one electron left in the ground $1s$ state. Here the notation A^{n+} relates to the ionization potential of the respective ion, so that after its ionization the ion with $z = n+1$ is produced.

nonrelativistically as long as the ionization potential is small compared to the rest energy of the electron, $I_p \ll c^2$. Quantitatively, relativistic effects in laser-induced tunneling are determined by the value of the parameter [31]

$$\xi^2 = 1 - \frac{1}{2}\epsilon[\sqrt{\epsilon^2+8} - \epsilon], \quad \epsilon = \frac{c^2 - I_p}{c^2}. \tag{4a}$$

In all the cases we consider here, it remains small, i.e.,

$$\xi^2 \approx \frac{2I_p}{3c^2} \ll 1. \tag{4b}$$

As an example, consider the ground $1s$ state of the Ar^{17+} ion with $I_p = 4426$ eV ≈ 163 a.u. Below we show that intensities $\mathcal{I} \approx 2\times10^{21}$ W/cm^2 are required to ionize this state producing bare Ar^{18+} ions. In this case $\xi^2 = 0.0058$, showing that the relativistic effect on the tunneling remains on the level of 1%. For intensities $\mathcal{I} \approx 10^{24}$ W/cm^2 and $I_p \approx 30$ keV (see Fig. 1), $\xi^2 \approx 0.04$, so that the nonrelativistic approximation remains quite accurate even at such otherwise ultrarelativistic intensities. This considerable extension of the nonrelativistic regime of tunneling toward ultrahigh intensities, roughly six orders in magnitude above that corresponding to $a_0 = 1$, where the electron motion becomes fully relativistic, can be qualitatively explained in the following way. The ionization event can be viewed as a detachment of the electron from its atomic orbital taking place at a distance of the order of the tunnel barrier width

$$b = \frac{I_p}{E_0} \gg a_B. \tag{5}$$

The electron covers this distance b during the time given by Eq. (3a), which is a small fraction of the laser period and can be estimated as

$$\tau_{\rm sb}\omega = \frac{\sqrt{I_p}\omega}{\sqrt{2}E_0} \equiv \frac{\gamma}{2} \ll 1. \tag{6}$$

Here the parameter γ, also known as the Keldysh parameter [35], is introduced. During this time interval the electron cannot be accelerated to relativistic kinetic energies, so that the magnetic component of the Lorentz force remains a small correction, unless the electron has had a relativistic velocity already in the beginning of its subbarrier motion. The latter is only possible for $I_p \simeq c^2$. As a result, at $\xi^2 \ll 1$ [see Eqs. (4a) and (4b)] the process of the electron's escape from an atom (ion) proceeds nonrelativistically.

(4) Finally, note that ionization occurs in a deep tunneling regime when the Keldysh parameter (6) is small. For a laser with wavelength $\lambda \simeq 1$ μm the value of (6) varies from $\gamma \simeq 10^{-2}$ for $\mathcal{I} = 10^{20}$ W/cm^2 and $I_p = 10^3$ eV to $\gamma < 10^{-3}$ for $\mathcal{I} = 10^{24}$ W/cm^2 and $I_p = 3\times10^4$ eV. This means that instantaneous static-field ionization rates are applicable for the calculation of the ionization probability. For the following, it will be useful to relate the laser electric field amplitude to the value of intensity expressed in units of 10^{20} W/cm^2. In this way the electric-field amplitude results, in atomic units, as

$$E_0 = \frac{53.4\sqrt{\mathcal{I}}}{\sqrt{1+\rho^2}}, \tag{7}$$

where ρ is the laser field ellipticity. In the following we consider linear polarization with $\rho = 0$.

B. Tunneling ionization rates

Under the assumptions formulated in the previous subsection, the ionization rate of a level in an ion with the residual charge z, i.e., $z = 1$ for neutral atoms and $z = N$ for ionization of an $A^{(N-1)+}$ ion, with the effective principal quantum number [31,32]

$$\nu = \frac{z}{\sqrt{2I_p}}, \tag{8}$$

and orbital and magnetic quantum numbers l and m, is given by the celebrated Perelomov-Popov-Terentiev (PPT) formula [28,31]:

$$w(\nu, l, m; t) = C_{\nu l}^2 B_{lm} I_p F^{1+|m|-2\nu}(t) \exp\left\{-\frac{2}{3F(t)}\right\}, \tag{9a}$$

with

$$C_{\nu l}^2 = \frac{2^{2\nu-2}}{\nu\Gamma(\nu+l+1)\Gamma(\nu-l)}, \tag{9b}$$

$$B_{lm} = \frac{(2l+1)(l+|m|)!}{2^{|m|}|m|!(l-|m|)!}, \tag{9c}$$

and the time-dependent reduced field $F(t)$ defined as

$$F(t) = \frac{\sqrt{\mathbf{E}_L^2(t)}}{(2I_p)^{3/2}}, \tag{10}$$

where $\mathbf{E}_L(t)$ is the laser electric field of the amplitude value E_0. The asymptotic coefficient C_{vl} in (9b) is taken in the approximate form introduced by Hartree [36].

By knowing the ionization rates, a system of rate equations determining populations $0 \leqslant c_z(t) \leqslant 1$ of different ionic states can be written in the form

$$\sum_z c_z(t) = 1, \tag{11a}$$

$$c_z(t) = \sum_{j,l} c_z(j,l;t), \tag{11b}$$

$$\frac{dc_z(j,l;t)}{dt} = \sum_{j',l'} c_{z-1}(j',l';t)\frac{n_{j',l'}}{2l'+1}\sum_{m'} w(\nu',l',m';t) - c_z(j,l;t)\frac{n_{j,l}}{2l+1}\sum_{m''} w(\nu,l,m'';t). \tag{11c}$$

Here the index j denotes the ionization pathway (see the Appendices for a more detailed explanation and examples), $c_z(j,l;t)$ are partial populations of orbitals with quantum number l along a fixed ionization pathway, and n_{jl} is the number of equivalent electrons at the orbital. The system of rate equations is truncated either at $z = Z$, where the Z is the atomic number of the element, or earlier if the intensity is not sufficient to fully ionize the atom. It can also be truncated from the side of small z, owing to the fact that all states with relatively small ionization potentials appear quickly depleted at high intensities. Truncated systems of rate equations for argon, krypton, and xenon are presented in the Appendices.

C. Intensity-dependent ionization offset

Before solving numerically the system (11a)–(11c), which is done in the next section, we derive an estimate for the maximal charge state which can be achieved via tunneling ionization for a given value of laser intensity. The purpose of this estimate is twofold. First, it allows for approximately finding, without demanding numerical calculations, the interval of charge states expected to be observed if the value of intensity is known, and vice versa. Secondly, and not less important, it will help us to considerably reduce the number of terms in the system defined in (11a)–(11c) by omitting those ones which, at a given intensity, correspond either to levels which are ionized quickly, so that for them $c_z = 0$ or, instead, to those which remain almost unaffected for the field, i.e., $c_z \approx 1$. For high-Z ions, where the number of rate equations becomes excessively large, this enormously simplifies the actual numerical calculations.

In order to estimate the maximal charge number which can be produced at a given intensity with a high probability, we discard the (l,m) dependence in Eq. (9a) and consider the total ionization probability per laser period for an s state at the maximal intensity (to simplify notations, we set time such that the maximum is achieved at $t = 0$):

$$W = \frac{2\pi}{\omega} w(\nu,0,0;0) = \pi C_\kappa^2 K_0 2^{2\nu+2} F^{1-2\nu} \exp\left\{-\frac{2}{3F}\right\}, \tag{12}$$

where $K_0 = I_p/\omega$ is the multiquantum parameter [31,32] and the reduced field F (10) is calculated for the amplitude value E_0 of the laser field. The exponential factor dominates the intensity dependence of the rate (12). For a given value of intensity (and therefore of E_0) we estimate the threshold ionization potential $I_p^*(\mathcal{I})$, such that the probability of ionization per laser cycle is of the order of unity, $W \simeq 1$. This condition is essentially approximate as it ignores the pulse duration, the (l,m) dependence, and the ionization saturation effect. However, thanks to the exponential factor in Eq. (12), which changes very rapidly with variations of the laser field amplitude, it provides a logarithmically accurate estimate:

$$F^* = \tfrac{2}{3}\ln^{-1}\left[2^{2\nu+2} C_\kappa^2 \pi K_0 (F^*)^{1-2\nu}\right]. \tag{13}$$

As is typical for logarithmic asymptotics, the denominator in the right-hand side (RHS) of Eq. (13) is a numerically large value of the order of 10. This gives the offset condition in the form (cf. [37]) $F^* \simeq 0.05$ or

$$I_p^* \simeq \tfrac{1}{2}(20E_0)^{2/3} \approx 52.2\mathcal{I}^{1/3}. \tag{14}$$

In Fig. 1 we show the dependence, Eq. (14), versus laser intensity. Several ionization potentials of noble gases (metals) are shown by horizontal solid (dashed) lines.

Note that the logarithmic factor in the denominator of Eq. (13) grows with intensity via the growth of the ionization potential and therefore the value of K_0. This leads to a further suppression of the threshold value F^* at higher intensities. Solving Eq. (13) numerically one may find that $F^* \approx 0.08$ for the ground state of hydrogen, while for Ar^{15+}, with $I_p = 918.3$ eV, $F^* \approx 0.03$. This leads to an important conclusion simplifying our calculations: ionic states with higher ionization potentials are efficiently ionized at lower reduced fields, which makes the sub-barrier tunneling mechanism of ionization more relevant than in the case of neutral atoms where one may enter the barrier suppression regime having $F^* \simeq 0.1$. For model analytic formulas describing multiple ionization in this intermediate regime see a recent paper [38].

The relativistic generalization of this result, which becomes quantitatively important at intensities exceeding 10^{24} W/cm^2, can be obtained by replacing Eq. (12) to its relativistic counterpart. The structure of the tunneling exponent remains the same with the difference that the characteristic field, Eq. (3c), is now determined as [31]

$$F_{\rm ch} = \frac{[\sqrt{3}\xi(I_p)]^3}{1+\xi^2(I_p)} c^3, \tag{15}$$

with $\xi^2(I_p)$ given by Eq. (4a). A calculation similar to that given above for the nonrelativistic limit leads to an implicit formula for the relativistic offset I_p^*

$$\mathcal{I} = 1.57\times 10^8 \frac{\xi^6(I_p^*)}{1+\xi^2(I_p^*)}, \tag{16}$$

which coincides with Eq. (14) for $I_p^* \ll c^2$. Accounting for the second term in the expansion of (4a) in powers of I_p/c^2, we obtain instead of Eq. (14)

$$I_p^* \approx 52.2\mathcal{I}^{1/3}(1 + 4.63 \times 10^{-4}\mathcal{I}^{1/3}). \tag{17}$$

The relativistic correction in Eq. (17) remains small even at 10^{24} W/cm^2, so that the two curves calculated along Eqs. (14) and (17) remain visually indistinguishable for the intensity interval shown in Fig. 1. Thus the nonrelativistic approximation for the ionization rate continues quantitatively correct at these intensities. A considerable difference between relativistic and nonrelativistic rates becomes apparent only at $\mathcal{I} \simeq 10^{26}$ W/cm^2. This remarkable extension of the nonrelativistic picture for the particular case of tunneling in a low frequency electromagnetic field deserves to be pointed out (see also a discussion in [31], where a comparison between the two rates is treated in a different way).

D. Effect of the intensity space distribution

The estimate (14) allows for deriving a universal approximate expression for the charge distribution of ions produced in the laser focus. To this end, we assume that an atom located at a point **r** will be ionized up to the charge corresponding to the value of ionization potential given by Eq. (14), which in turn depends on the local maximal value of intensity $\mathcal{I}(\mathbf{r})$. This model presumes that the pulse duration is sufficient to strip out all levels with lower I_p's before the field reaches its maximum. In the next section we check the validity of this approximation by solving numerically a system of rate equations (11a)–(11c) for different ionic species. For the time being, we consider I_p as a continuous value. Then, the number of ions with ionization potentials in the interval dI_p is given by

$$dN = -n_0 \frac{dV}{dI_p} dI_p = 3n_0 \frac{I_p^2}{I_{pm}^{*3}} \frac{dV}{d\delta} dI_p, \quad \delta = \frac{\mathcal{I}}{\mathcal{I}_m}. \tag{18}$$

Here $\mathcal{I}_m$ is the peak intensity value in the focus and I_{pm}^* is the corresponding offset ionization potential given by Eq. (14). The space volume with intensity equal to or exceeding $\mathcal{I}$ is denoted as $V(\delta)$:

$$V(\delta) = \int_{\delta \leqslant \delta'(\mathbf{r}) \leqslant 1} d^3 r. \tag{19}$$

For the simplest case of a fundamental Gaussian beam symmetric with respect to the x axis,

$$\mathcal{I}(r_\perp, x) = \frac{\mathcal{I}_m}{1 + x^2/x_R^2} \exp\left\{ - \frac{2r_\perp^2}{w_0^2(1 + x^2/x_R^2)} \right\}, \tag{20}$$

with $x_R = \pi w_0^2/\lambda$ being the Rayleigh length and w_0 the focal waist, a trivial calculation gives

$$V(\delta) = \frac{4\pi^2}{3} \frac{w_0^4}{\lambda} \left\{ \frac{1}{6} y^3 + y - \mathrm{atan}(y) \right\},$$
$$y = \sqrt{\frac{1}{\delta} - 1} = \sqrt{\frac{\mathcal{I}_m}{\mathcal{I}} - 1}, \tag{21}$$

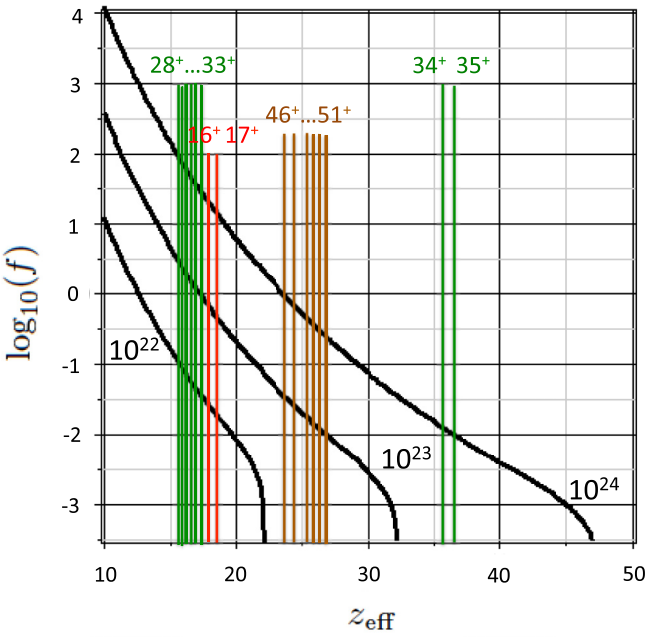

FIG. 2. Charge distributions (22) (in logarithmic scale) calculated for $\mathcal{I}_m = 10^{22}$ W/cm^2, 10^{23} W/cm^2, and 10^{24} W/cm^2 as functions of the effective charge $z_{\mathrm{eff}} = \sqrt{2I_p}$. The distributions are shown by thick black lines with the values of intensity indicated near each curve. Selected charge states of argon, krypton, and xenon are shown by vertical red, green, and brown lines, respectively. The value at the intersection of vertical lines with the distributions approximately indicates the relative amount of the respective charge state at a given intensity.

so that the distribution in ionization potentials (18) takes the form

$$f(I_p, \mathcal{I}_m) \equiv \frac{dN}{dI_p} = \frac{\pi^2 n_0 w_0^4}{\lambda I_p} \sqrt{\frac{\mathcal{I}_m}{\mathcal{I}} - 1} \left(2 + \frac{\mathcal{I}_m}{\mathcal{I}} \right). \tag{22}$$

The distribution is divergent at $I_p \to 0$ due to the formally unlimited focal volume. This makes, however, no difficulty for practical calculations, as the effective volume is restricted either by the minimal value of the ionization potential of a neutral gas or by the geometry of a TOF detector [39].

Figure 2 shows the distribution (22) for several values of the peak focus intensity, as a function of the effective ion charge $z_{\mathrm{eff}} = \sqrt{2I_p}$, equal to the charge of a hydrogenlike ion having the same ionization potential. Values of z_{eff} for several charge states in argon, krypton, and xenon are indicated by vertical lines to reproduce realistic discrete charge distributions. In order to estimate a relative amount of different charge states one has to look at intersections of vertical lines with the respective distribution curve. As an example, for ionization of krypton at $\mathcal{I} = 10^{24}$ W/cm^2 the number of Kr^{35+} and Kr^{36+} ions in the focus is expected to be approximately 3.5–4.0 orders of magnitude less than that of Kr^{29+}–Kr^{34+} ions. Instead, for ionization of xenon at $\mathcal{I} = 10^{23}$ W/cm^2 the number of Xe^{47+} ions is expected to be roughly three times more than that of Xe^{52+}, while Xe^{53+} and Xe^{54+} will not be produced at this intensity.

More precisely, the number of A^{n+} ions produced in the focus at a given $\mathcal{I}_m$ is obtained by calculating the area

under the respective curve between the ionization potentials of $A^{(n-1)+}$ and A^{n+}. Using Eq. (21) this number can be explicitly expressed as

$$N(A^{n+}) = n_0\{V(I_p(A^{(n-1)+})) - V(I_p(A^{+}))\} \approx \frac{\pi^2 n_0 w_0^4}{\lambda}\sqrt{\frac{\mathcal{I}_m}{\mathcal{I}} - 1}\left(2 + \frac{\mathcal{I}_m}{\mathcal{I}}\right)\frac{\Delta I_p}{I_p}. \quad (23)$$

Here $\Delta I_p = I_p(A^{n+}) - I_p(A^{(n-1)+})$, $I_p = I_p(A^{(n-1)+})$, and $\mathcal{I} = \mathcal{I}(I_p)$ calculated from (14). For the case of a fully stripped atom, i.e., for $n = Z$, the value of $I_p(A^{n+})$ does not exist; therefore, Eq. (23) has to be modified by replacing $I_p(A^{n+}) \to I^*_{pm}$. In particular, this formula allows for estimating the absolute number of ions $N(A^{n+})$ produced in the focus, which is crucial to check the experimental availability to detect these ions. As an example, taking krypton at an intensity 3×10^{23} W/cm^2, which is approximately 1.5 higher than the threshold intensity for Kr^{35+} (see Fig. 1), using $I_p(Kr^{35+}) \approx 17936$ eV [40], and assuming $n_0 = 10^{13}$ cm^{-3}, $\lambda = 1$ μm, and $w_0 \approx 2\lambda$, we estimate $N(Kr^{36+}) \approx 80$, which should be sufficient for detection.

III. NUMERICAL RESULTS

In this section, we numerically verify the theory introduced above. In order to find the distribution of ionic charge states during and after the interaction with intense laser radiation, we solve a set of equations (11a)–(11c) using the nonrelativistic static rates, Eq. (9a), for argon, krypton, and xenon in different ranges of laser intensities. We employ an adaptive stepsize Runge-Kutta scheme, based on the Numerical Recipes [41].

In a fully rigorous calculation, one should start the simulation from a neutral atom and take into account all possible trees of ionic states which develop starting from this initial condition. A simple analysis shows, however, that the number of possible pathways grows enormously as the maximal charge number increases. Even reasonably assuming that (a) there is no ionization from inner shells until the outer shell is not fully striped out of electrons, (b) ionization proceeds without excitation of the residual ion, and (c) one neglects the fine structure of electronic terms, we obtain that the number of pathways for ionization of argon is equal to $P = 1$ for initial states Ar^{n+} with $n \geqslant 14$, $P = 6$ for $n = 12$, $P = 28$ for $n = 8$, etc. Calculation of P for the initial configuration $1s^2 2s^2 2p^6$

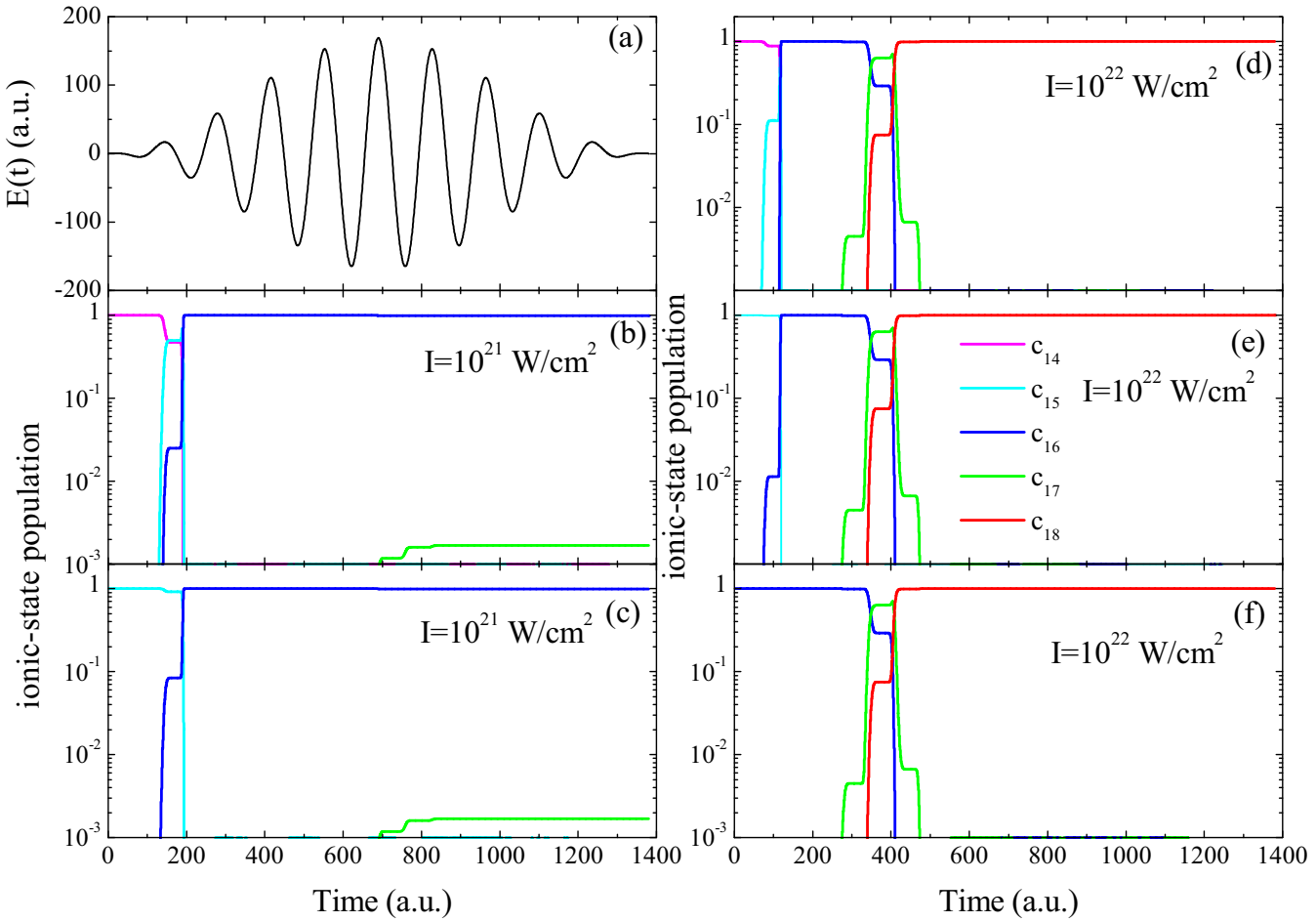

FIG. 3. (a) Time profile of the laser electric field for an equivalent laser intensity $\mathcal{I}_m = 10^{21}$ W/cm^2; (b)–(f) populations c_n for Ar^{n+} ions as a function of time calculated by solving numerically the system of rate equations (B1)–(B5). For (b) and (c) the laser intensity is set to $\mathcal{I}_m = 10^{21}$ W/cm^2 and for (d)–(f) to $\mathcal{I}_m = 10^{22}$ W/cm^2. The initial conditions are (b) $c_{14}(0) = 1$, $c_{15}(0) = \cdots = c_{18}(0) = 0$, (c) $c_{14}(0) = 0$, $c_{15}(0) = 1$, $c_{16}(0) = \cdots = c_{18}(0) = 0$, (d) $c_{14}(0) = 1$, $c_{15}(0) = \cdots = c_{18}(0) = 0$, (e) $c_{14}(0) = 0$, $c_{15}(0) = 1$, $c_{16}(0) = \cdots = c_{18}(0) = 0$, and (f) $c_{14}(0) = c_{15}(0) = 0$, $c_{16}(0) = 1$, $c_{17}(0) = c_{18}(0) = 0$.

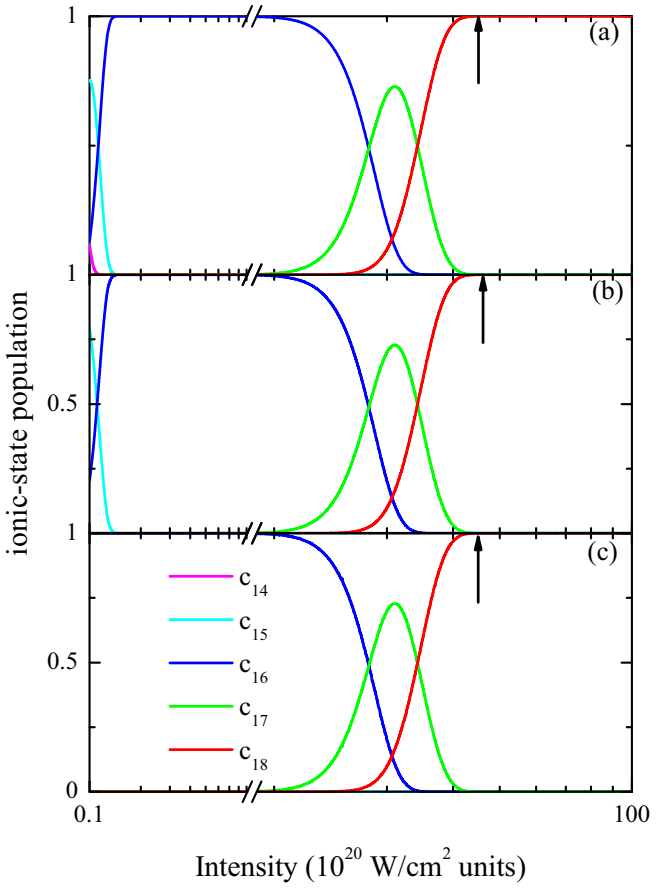

FIG. 4. Populations c_n for Ar^{n+} ions at the end of the laser pulse as functions of the laser peak intensity. The initial conditions are (a) $c_{14}(0) = 1$, $c_{15}(0) = \cdots = c_{18}(0) = 0$, (b) $c_{14}(0) = 0$, $c_{15}(0) = 1$, $c_{16}(0) = \cdots = c_{18}(0) = 0$, and (c) $c_{14}(0) = c_{15}(0) = 0$, $c_{16}(0) = 1$, $c_{17}(0) = c_{18}(0) = 0$. Arrows mark the saturation intensities which have to be compared with those extracted from Eq. (14) or Fig. 1. Note that here we point out the saturation intensity needed to generate bare ions, which corresponds, in notations of Fig. 1, to the ionization potential of $A^{(N-1)+}$ ions.

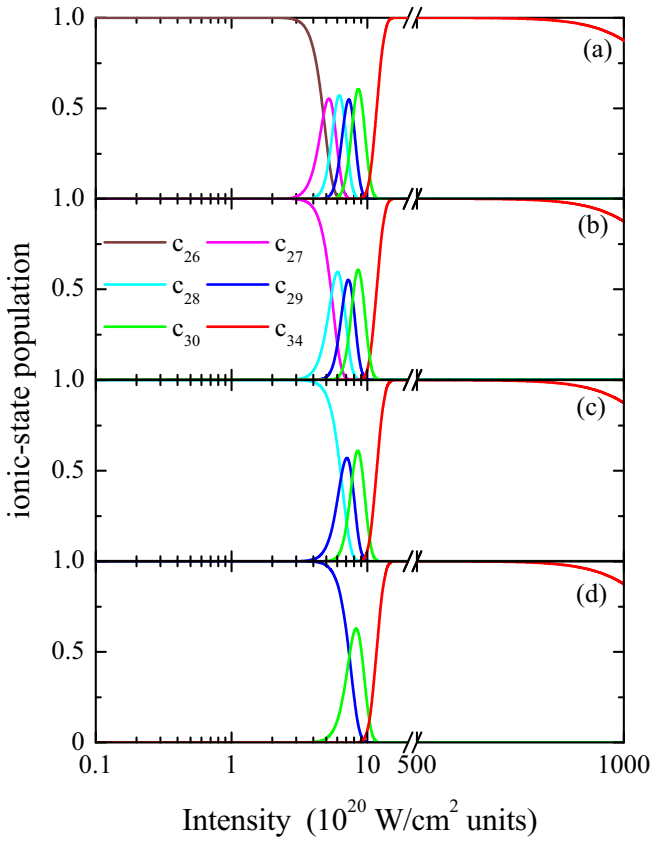

FIG. 5. Populations c_n for Kr^{n+} ions at the end of the laser pulse as functions of the laser peak intensity for the case (a) (see Appendix B for details). The initial conditions are (a) $c_{26}(0) = 1$, $c_{27}(0) = \cdots = c_{33}(0) = 0$, (b) $c_{26}(0) = 0$, $c_{27}(0) = 1$, $c_{28}(0) = \cdots = c_{34}(0) = 0$, (c) $c_{26}(0) = c_{27}(0) = 0$, $c_{28}(0) = 1$, $c_{29}(0) = \cdots = c_{34}(0) = 0$, and (d) $c_{26}(0) = \cdots = c_{28}(0) = 0$, $c_{29}(0) = 1$, $c_{30}(0) = \cdots = c_{34}(0) = 0$. For clarity, only the relevant ionic state populations are plotted. The saturation intensity for ionization of Kr^{34+} ions lies beyond $\mathcal{I} = 10^{23}$ W/cm^2 [see Fig. 1 and Eq. (14)].

(corresponding to neutral neon, Ar^{8+}, etc.), based on these simplifications, is explained in Appendix A.

The analytical estimates of previous sections allow one to substantially reduce the complexity of the problem. This is so by assuming that ionization starts from ionic charge states whose ionization potential can be estimated from Eq. (14), while all the outermost levels have been quickly ionized before the peak value of intensity has been reached. Thus our numerical calculation intends to show the ionization dynamics of levels with ionization potentials not very much different from those given by Eq. (14). Such calculation will verify the accuracy of the analytic estimate and show how quickly ionization saturation can be achieved at a fixed laser intensity.

For distinctness, we suppose that an experiment aims probing laser intensities in the interval $\mathcal{I}_m = 10^{21}$–10^{23} W/cm^2 at the center of the focus. According to Fig. 1, in this interval one would expect significant production of Ar^{18+} (bare argon nucleus) and Kr^{28+}–Kr^{34+} ions. Ionic states with lower ionization potentials will be quickly ionized during the pulse intensity growth, while the probability of production of Kr^{35+}–Kr^{36+} will remain negligibly small in this range of intensities. In order to check these qualitative predictions, we solve the associated systems of rate equations for Ar and Kr in a spatially homogeneous linearly polarized laser pulse. In this case the time-dependent laser electric field $E(t)$ takes the form

$$E(t) = E_L f(t) \cos(\omega t), \tag{24}$$

where the pulse envelope is defined as $f(t) = \sin^2(\frac{\omega t}{2N})$, with N the total number of optical cycles. In our simulations we use $\omega = 0.0455$ a.u. and $N = 10$, that correspond to a laser wavelength $\lambda = 1$ μm and a total pulse length $T \sim 33$ fs, respectively.

We consider the following assumptions.

(a) The initial state is chosen to have considerably lower ionization potential than $I_p^*(\mathcal{I}_{\max})$, but high enough to minimize the number of rate equations in the system. For practical calculations, we set up for the initial condition a gas of A^{k+} with k determined from Eq. (14) with intensity two orders

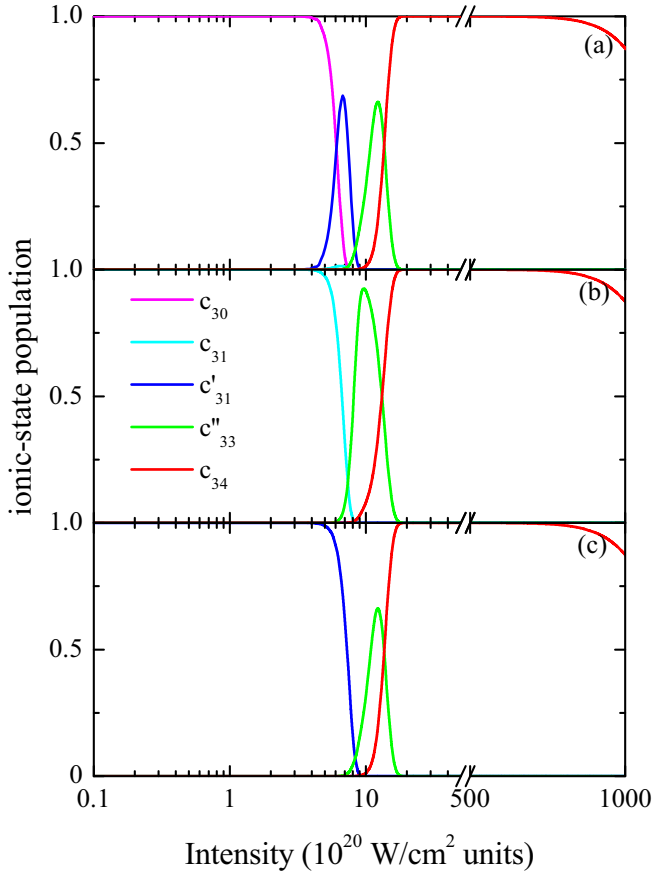

FIG. 6. Populations c_n for Kr^{n+} ions at the end of the laser pulse as functions of the laser peak intensity for the case (b) (see Appendix B for details). The initial conditions are (a) $c_{30}(0) = 1,\ c_{31}(0) = \cdots = c_{34}(0) = 0$, (b) $c_{30}(0) = 0,\ c_{31}(0) = 1,\ c'_{31}(0) = \cdots = c_{34}(0) = 0$, and (c) $c_{30}(0) = c_{31}(0) = 0,\ c'_{31}(0) = 1,\ c_{32}(0) = \cdots = c_{34}(0) = 0$. For clarity, only the relevant ionic states populations are plotted. The saturation intensity for ionization of Kr^{34+} ions lies beyond $\mathcal{I} = 10^{23}$ W/cm^2 [see Fig. 1 and Eq. (14)].

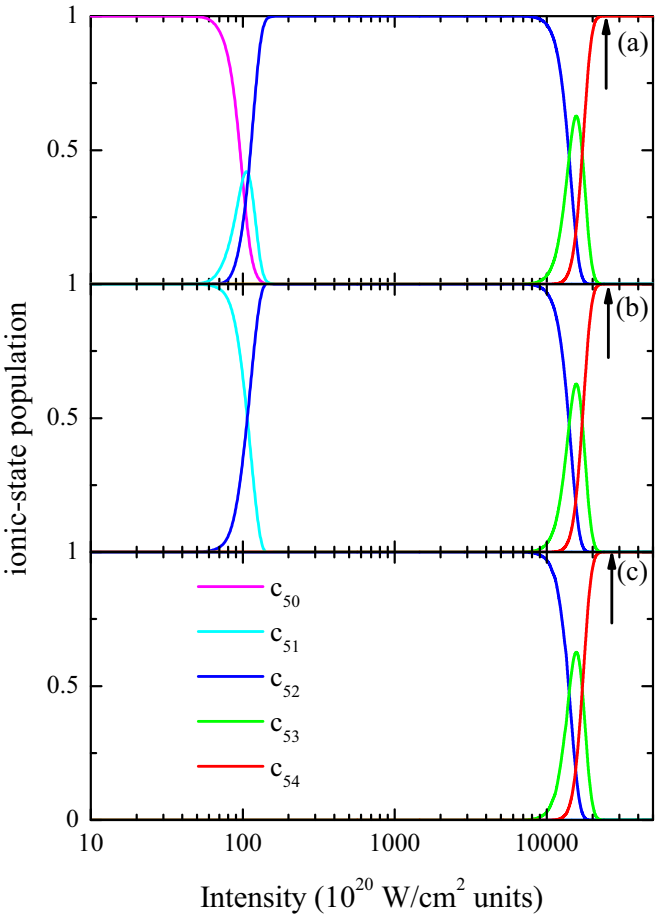

FIG. 7. Populations c_n for Xe^{n+} ions at the end of the laser pulse as functions of the laser peak intensity. The initial conditions are (a) $c_{50}(0) = 1,\ c_{51}(0) = \cdots = c_{54}(0) = 0$, (b) $c_{50}(0) = 0,\ c_{51}(0) = 1, c_{52}(0) = \cdots = c_{54}(0) = 0$, and (c) $c_{50}(0) = c_{51}(0) = 0,\ c_{52}(0) = 1,\ c_{53}(0) = c_{54}(0) = 0$. Arrows mark the saturation intensities which have to be compared with those extracted from Eq. (14).

in magnitude below the peak intensity under consideration. As an example, considering ionization by pulses with $\mathcal{I}_m = 10^{21}$ W/cm^2 we assume a first set of calculations setting $c_{14}(0) = 1$ for argon (see below for more details). In order to justify the validity of such model initial conditions, we ran several calculations with different initial ionic states and confirmed that the final ionic states distribution remains insensitive to the initial choice.

(b) Ionization is not followed by excitation of the residual ion. This assumption is amply justified by the deep tunnel regime of ionization we consider, when the Keldysh parameter in Eq. (6) remains well below 0.1. However, this assumption does not imply that an electron with a slightly higher ionization potential cannot be removed before that with a smaller one, provided the difference between the ionization potentials is relatively not too high. This may happen for shells containing s and p electrons, as illustrated in Appendix A.

Assumptions (a) and (b) further reduce the number of rate equations in the system. For simulations, we take the data on ionization potentials and (l, m) configurations of ionic levels in argon, krypton, and xenon from the fundamental works by Saloman [40,42,43]. We first calculate the dependence on time of the populations $c_{14} \ldots c_{18}$ for argon in the field (24) with two different peak intensities: 10^{21} W/cm^2 and 10^{22} W/cm^2. The results are shown in Fig. 3, where the populations $c_{14} \ldots c_{18}$ are present for different initial conditions assuming that the preionized gas consists of Ar^{14+} [Figs. 3(b)–3(d)], Ar^{15+} [Figs. 3(c)–3(e)], and Ar^{16+} [Fig. 3(f)], respectively. In Figs. 3(b) and 3(c) the laser intensity is 10^{21} W/cm^2; meanwhile, in Figs. 3(d)–3(f) we set the laser intensity at 10^{22} W/cm^2. We expect the subcycle time dynamics of the ionic-state populations will indeed be sensitive to the pulse shape, i.e., the curves of Figs. 3(b)–3(f) should change if we model the laser pulse shape as a Gaussian or sech^2, but the final state values will not. As we are interested in the ionic-state populations at the end of the laser pulse, its shape is hardly relevant. In any case, in a detailed simulation, aimed to compare with experimental data, we will employ a more realistic pulse shape. By addressing Figs. 1 and 2, one has to note that there ionization potentials of the respective ions

are shown, while the coefficients c_n describe populations of states generated in the process of ionization of these ions. As a result, the value of index n on Figs. 1 and 2 and Figs. 3–7 differs by 1.

In Fig. 4 we plot the ionic states of Ar at the end of the laser pulse as a function of the laser intensity in a range of 10^{19}–10^{22} W/cm^2. We employ three different initial conditions, namely $c_{14}(0) = 1$, $c_{15}(0) = \cdots = c_{18}(0) = 0$ [Fig. 4(a)], $c_{14}(0) = c_{16}(0) = \cdots = c_{18}(0) = 0$, $c_{15}(0) = 1$ [Fig. 4(b)], and $c_{14}(0) = c_{15}(0) = 0$, $c_{16}(0) = 1$, $c_{17}(0) = c_{18}(0) = 0$ [Fig. 4(c)] (see Appendix B for more details). Here the rates $w(\nu_z, l, m; t)$ are found from Eq. (9a) with the effective principal quantum numbers $\nu_{14} = 1.89$, $\nu_{15} = 1.95$, $\nu_{16} = 0.98$, and $\nu_{17} = 1.00$ calculated from Eq. (8), using the ionization potentials taken from [42].

Several conclusions can be drawn at this point. First, the results shown in Figs. 3 and 4 fully support assumption (a): the final distribution of charge states appears insensitive to the initial state, provided its ionization potential is low enough. In this case solutions corresponding to different initial states appear almost indistinguishable. Second, and even more important, the plots of Figs. 3 and 4 show the reliability of the analytic estimations given by Eq. (14). The charge state Ar^{16+} is reached at $\mathcal{I} \approx 1.3 \times 10^{19}$ W/cm^2 and Ar^{18+} at $\mathcal{I} \approx 4 \times 10^{21}$ W/cm^2, in a reasonable agreement with the analytic estimates. The latter assumes that, as the value of intensity grows, populations of charge states evolve from zero to 1 and then back to zero in small intensity intervals, so that the coefficients c_n can be approximated by Heaviside functions. As is seen from the curves of Figs. 3 and 4, populations of the levels behave almost as step functions, justifying the validity of the latter approximation.

A similar calculation was performed for krypton taking as the initial condition ionic states between Kr^{26+} and Kr^{31+} and in an intensity range between 10^{19} W/cm^2 and 10^{23} W/cm^2. In the first case we have taken into account only one pathway corresponding to the removal of the outermost electron always, i.e., the p electrons are removed first. This pathway is shown by red arrows on Fig. 8. In the second case all six relevant pathways are taken into account. The systems of rate equations are given in Appendix B. The corresponding distributions of the relevant ionic populations are shown on Figs. 5 and 6. We can observe that, as in the case of Ar, the final ionic state is independent of the initial condition. Interestingly, this behavior remains even when (i) we include excited states [case (b)] and (ii) we employ a completely different pathway to reach the same final state [compare the set of rate equations (B6)–(B14) with (B15)–(B23), Appendix B].

Finally, and for completeness, Fig. 7 shows the populations of Xe ions at the end of the laser pulse as a function of the laser intensity in a range 10^{21}–5×10^{24} W/cm^2. In Fig. 7(a) we start our simulations with $c_{50}(0) = 1$, $c_{51}(0) = \cdots = c_{54}(0) = 0$, in Fig. 7(b) with $c_{50}(0) = 0$, $c_{51}(0) = 1$, $c_{53}(0) = \cdots = c_{54}(0) = 0$, and in Fig. 7(c) with $c_{50}(0) = 0$, $c_{51}(0) = 0$, $c_{52}(0) = 1$, $c_{53}(0) = c_{54}(0) = 0$. As in the previous case, we observe a very good agreement between the saturation intensities obtained numerically with the analytical estimates derived from Eq. (14).

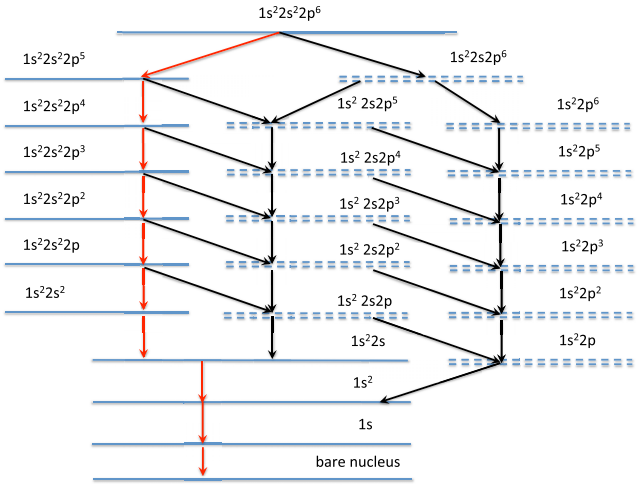

FIG. 8. Substructure of levels and ionization pathways making the main contribution into sequential multiple ionization of atomic systems prepared in the ground $1s^2 2s^2 2p^6$ state. Ground and excited states are shown by blue solid and dashed lines correspondingly. Most of the excited states consist of several sublevels with different values of the full angular momentum J. The ionization pathway which involves only the ground states is shown by red arrows; all other pathways are shown by black arrows.

IV. CONCLUSIONS AND PERSPECTIVES

In conclusion, we have demonstrated that using the strong dependence of the ionization offset in complex atoms on laser intensity the latter can be reliably estimated. The simple analytic estimates of Sec. II qualitatively agree with the numerical results of Sec. III. The former help in identifying intervals of ionization potentials necessary to probe a certain range of laser intensities, but do not provide quantitative accuracy. Therefore, for a precise determination of the maximal laser intensity in the focus, numerical solution of the rate equations is required along the lines presented in Sec. III and Appendix B.

Two significant experimental-related issues will probably be faced on the way to an implementation of this diagnostic. First, a spatial distribution of laser intensity in the focus will lead to the volume effect analytically examined in Sec. II D resulting in production of a very significant number of relatively low charged ions which can saturate the signal recorded by the TOF detector. This problem can be resolved by mechanically restricting the effective volume accessible for the detector or by deflecting ions with sufficiently low charge states in a magnetic field before these ions reach the detector. Second, as discussed in Sec. II and shown by Fig. 1, there are large gaps in ionization potentials (and, correspondingly, an impossibility to estimate intensities in these regions) which cannot be filled in by noble gases, which are the most common elements being used as gas targets in strong field physics. Possible candidates, most likely highly charged ions of metals, such as Ag, Mo, Cu, etc., have to be examined in virtue of their feasibility for such an experiment.

ACKNOWLEDGMENTS

The authors acknowledge fruitful discussions with G. Paulus, B. Walker, and D. Batheja, S.V.P. thanks the

ELI-Beamlines for its kind hospitality and the Russian Foundation for Basic Research for financial support via Grant No. 19-02-00643. This work was supported by the project High Field Initiative (No. CZ.02.1.01/0.0/0.0/15_003/0000449) from European Regional Development Fund (HIFI) and by the project Advanced research using high intensity laser produced photons and particles (No. CZ.02.1.01/0.0/0.0/16_-019/0000789) from European Regional Development Fund (ADONIS).

APPENDIX A: IONIZATION CASCADES

Starting from a given ground state of an atom or an ion, ionization can proceed along different pathways. Clearly, for multielectron atoms the total number of such paths grows very quickly with the atomic number. Most of them do not give any considerable contribution into the production of ionic states owing to the structure of the tunneling rate. The tunneling exponent in Eq. (9a) is maximal for the outermost electron which has the minimal ionization potential. This makes ionization of inner shells highly improbable before the outer shells have been stripped out, so that such ionization pathways can be safely discarded. However, when electrons are being removed from the same shell, ionization of lower s levels may proceed with comparable or even higher probability than that of p levels with lower ionization potentials. The reasons for that are (a) a smaller value of the asymptotic coefficients C_{nl}^2 in Eq. (9b) and (b) the factor $F^{|m|}$ in Eq. (9a), which is small for nonzero magnetic quantum numbers, owing to the condition $F \ll 1$. As an example, for Kr^{26+} with the ground-state configuration $1s^2 2s^2 2p^6$, ionization of a p electron with $I_p \approx 2929$ eV proceeds with probability comparable to that for an s electron whose ionization potential is by $\Delta I_p \approx 235$ eV higher [40]. Indeed, taking $F \simeq F^* = 0.05$, one obtains that the tunneling exponent for the p electron is $\exp(\Delta I_p/I_p F) \approx 5$ times higher than that for the s electron. At the same time, for the latter $C_{n0}^2 = 1.088$, $B_{00} = 1$, while for the p electron $C_{n1}^2 = 0.315$ and $B_{10} = 3$, $B_{1\pm1} = 3/2$, and finally the factor $F^{|m|}$ gives 0.05 for $m = \pm 1$. Thus the p-state rate averaged over the magnetic quantum number appears only five times greater than that of the s state. For partially stripped p shells the difference in ionization potentials appears to be even smaller, so that, for configurations $2s^2 2p$ or $2s^2 2p^2$, the s and p rates are almost equal. These estimates show that the described submanifold of pathways may play an essential role in the ionization dynamics.

An example of the structure of levels is shown on Fig. 8 for the initial configuration $1s^2 2s^2 2p^6$, which corresponds to the neutral neon, Ar^{8+}, Kr^{26+}, etc.

For the initial configuration shown on Fig. 8 the total number of pathways is equal to 28. For the $1s^2 2s^2 2p^2$ configuration only six relevant pathways are left; starting from the $1s^2 2s^2$ configuration ionization proceeds along the unique pathway.

APPENDIX B: SYSTEMS OF RATE EQUATIONS

We solve numerically the system of rate equations for argon in the interval of intensities $\mathcal{I}_m = 10^{19}$–10^{22} W/cm^2, for krypton between $\mathcal{I}_m = 10^{19}$–10^{23} W/cm^2, and for xenon between $\mathcal{I}_m = 10^{21}$–5×10^{24} W/cm^2 using an adaptive step-size Runge-Kutta scheme [41]. We start with the simplest configuration $1s^2 2s^2$ for argon (Ar^{14+}, $I_p \approx 855$ eV). The value of I_p is well below that of Eq. (14) for 10^{20} W/cm^2, which is $I_p^* \approx 1420$ eV. For this initial configuration, only one relevant pathway contributes (see Fig. 8 and Appendix A). The resulting system of rate equations is therefore particularly simple and reads

$$\frac{dc_{14}}{dt} = -2c_{14} w(\nu_{14}, 0, 0; t), \tag{B1}$$

$$\frac{dc_{15}}{dt} = 2c_{14} w(\nu_{14}, 0, 0; t) - c_{15} w(\nu_{15}, 0, 0; t), \tag{B2}$$

$$\frac{dc_{16}}{dt} = c_{15} w(\nu_{15}, 0, 0; t) - 2c_{16} w(\nu_{16}, 0, 0; t), \tag{B3}$$

$$\frac{dc_{17}}{dt} = 2c_{16} w(\nu_{16}, 0, 0; t) - c_{17} w(\nu_{17}, 0, 0; t), \tag{B4}$$

$$\frac{dc_{18}}{dt} = c_{17} w(\nu_{17}, 0, 0; t). \tag{B5}$$

Coefficients 2 in Eqs. (B1)–(B4) are due to the presence of two equivalent electrons in the subshell.

For the interval of intensities used for Kr, the system of rate equations has to include p states of the $2p$ shell. In order to simplify the calculations, we consider two cases: (a) the $1s^2 2s^2 2p^6$ state as initial configuration, with only the most probably pathway accounted for (shown on Fig. 8 by red arrows) and (b) the $1s^2 2s^2 2p^2$ as initial configuration with all relevant pathways accounted for (shown on Fig. 8 by red and black arrows). For case (a) the system explicitly reads

$$\frac{dc_{26}}{dt} = -2c_{26}\{w(\nu_{26}, 1, 0; t) + 2w(\nu_{26}, 1, \pm1; t)\}, \tag{B6}$$

$$\frac{dc_{27}}{dt} = 2c_{26}\{w(\nu_{26}, 1, 0; t) + 2w(\nu_{26}, 1, \pm1; t)\} - \frac{5}{3}c_{27}\{w(\nu_{27}, 1, 0; t) + 2w(\nu_{27}, 1, \pm1; t)\}, \tag{B7}$$

$$\frac{dc_{28}}{dt} = \frac{5}{3}c_{27}\{w(\nu_{27}, 1, 0; t) + 2w(\nu_{27}, 1, pm1; t)\} - \frac{4}{3}c_{28}\{w(\nu_{28}, 1, 0; t) + 2w(\nu_{28}, 1, \pm1; t)\}, \tag{B8}$$

$$\frac{dc_{29}}{dt} = \frac{4}{3}c_{28}\{w(\nu_{28}, 1, 0; t) + 2w(\nu_{28}, 1, \pm1; t)\} - c_{29}\{w(\nu_{29}, 1, 0; t) + 2w(\nu_{29}, 1, \pm1; t)\}, \tag{B9}$$

$$\frac{dc_{30}}{dt} = c_{29}\{w(\nu_{29}, 1, 0; t) + 2w(\nu_{29}, 1, \pm1; t)\} - \frac{2}{3}c_{30}\{w(\nu_{30}, 1, 0; t) + 2w(\nu_{30}, 1, \pm1; t)\}, \tag{B10}$$

$$\frac{dc_{31}}{dt} = \frac{2}{3}c_{30}\{w(\nu_{30}, 1, 0; t) + 2w(\nu_{30}, 1, \pm1; t)\} - \frac{1}{3}c_{31}\{w(\nu_{31}, 1, 0; t) + 2w(\nu_{31}, 1, \pm1; t)\}, \tag{B11}$$

$$\frac{dc_{32}}{dt} = \frac{1}{3}c_{31}\{w(\nu_{31},1,0;t) + 2w(\nu_{31},1,\pm1;t)\} - 2c_{32}w(\nu_{32},0,0;t), \quad \text{(B12)}$$

$$\frac{dc_{33}}{dt} = 2c_{32}w(\nu_{32},0,0;t) - c_{33}w(\nu_{33},0,0;t), \quad \text{(B13)}$$

$$\frac{dc_{34}}{dt} = c_{33}w(\nu_{33},0,0;t) - 2c_{34}w(\nu_{34},0,0;t). \quad \text{(B14)}$$

The system can be safely truncated by Eq. (B14), as the ionization potential of Kr^{34+}, $I_p = 17296$ eV, is too high to expect any considerable ionization below 10^{23} W/cm^2 (see Figs. 1 and 2). The effective principal quantum numbers ν_z are calculated using data from [40].

For case (b) we take into account all relevant pathways (see red and black arrows in Fig. 8) up to the same ionic state as the one used in (a). As a result, excited states of two types, $1s^22s2p^n$ and $1s^22p^n$ with $n = 1, 2$, enter in the calculation. We denote the values corresponding to these two sets of excited states by one and two primes, respectively. Then the system of rate equations reads

$$\frac{dc_{30}}{dt} = -c_{30}\left\{\frac{2}{3}[w(\nu_{30},1,0;t) + 2w(\nu_{30},1,\pm1;t)] + 2w(\nu'_{30},0,0;t)\right\}, \quad \text{(B15)}$$

$$\frac{dc_{31}}{dt} = -c_{31}\left\{\frac{1}{3}[w(\nu_{31},1,0;t) + 2w(\nu_{31},1,\pm1;t)] + 2w(\nu'_{31},0,0;t)\right\} + c_{30}\frac{2}{3}[w(\nu_{30},1,0;t) + 2w(\nu_{30},1,\pm1;t)], \quad \text{(B16)}$$

$$\frac{dc'_{31}}{dt} = -c'_{31}\left\{\frac{2}{3}[w(\nu'_{31},1,0;t) + 2w(\nu'_{31},1,\pm1;t)] + w(\nu''_{31},0,0;t)\right\} + 2c_{30}w(\nu'_{30},0,0;t), \quad \text{(B17)}$$

$$\frac{dc_{32}}{dt} = -2c_{32}w(\nu_{32},0,0;t) + c_{31}\left\{\frac{1}{3}[w(\nu_{31},1,0;t) + 2w(\nu_{31},1,\pm1;t)]\right\}, \quad \text{(B18)}$$

$$\frac{dc'_{32}}{dt} = -c'_{32}\left\{\frac{1}{3}[w(\nu'_{32},1,0;t) + 2w(\nu'_{32},1,\pm1;t)] + w(\nu''_{32},0,0;t)\right\} + 2c_{31}w(\nu'_{31},0,0;t) + c'_{31}\left\{\frac{2}{3}[w(\nu'_{31},1,0;t) + 2w(\nu'_{31},1,\pm1;t)]\right\}, \quad \text{(B19)}$$

$$\frac{dc''_{32}}{dt} = -\frac{2}{3}c''_{32}[w(\nu''_{32},1,0;t) + 2w(\nu''_{32},1,\pm1;t)] + c'_{31}w(\nu''_{31},0,0;t), \quad \text{(B20)}$$

TABLE I. Parameters for the first ionization cascade of Kr.

Ionic state	e configuration	I_p (eV)	ν	C^2	l	m	B_{lm}
Kr^{26+}	$1s^22s^22p^6$	2 929	1.840	0.315	1	0	3
Kr^{26+}	$1s^22s^22p^6$	2 929	1.840	0.315	1	±1	3/2
Kr^{27+}	$1s^22s^22p^5$	3 072	1.863	0.319	1	0	3
Kr^{27+}	$1s^22s^22p^5$	3 072	1.863	0.319	1	±1	3/2
Kr^{28+}	$1s^22s^22p^4$	3 238	1.882	0.321	1	0	3
Kr^{28+}	$1s^22s^22p^4$	3 238	1.882	0.321	1	±1	3/2
Kr^{29+}	$1s^22s^22p^3$	3 381	1.903	0.322	1	0	3
Kr^{29+}	$1s^22s^22p^3$	3 381	1.903	0.322	1	±1	3/2
Kr^{30+}	$1s^22s^22p^2$	3 584	1.910	0.325	1	0	3
Kr^{30+}	$1s^22s^22p^2$	3 584	1.910	0.325	1	±1	3/2
Kr^{31+}	$1s^22s^22p$	3 752	1.927	0.327	1	0	3
Kr^{31+}	$1s^22s^22p$	3 752	1.927	0.327	1	±1	3/2
Kr^{32+}	$1s^22s^2$	3 971	1.931	1.030	0	0	1
Kr^{33+}	$1s^22s$	4 108	1.956	1.029	0	0	1
Kr^{34+}	$1s^2$	17 296	0.981	0.990	0	0	1
Kr^{35+}	$1s$	17 936	0.995	0.995	0	0	1

$$\frac{dc_{33}}{dt} = -c_{33}w(\nu_{33},0,0;t) + 2c_{32}w(\nu_{32},0,0;t) + \frac{1}{3}c'_{32}[w(\nu'_{32},1,0;t) + 2w(\nu'_{32},1,\pm1;t)], \quad \text{(B21)}$$

$$\frac{dc''_{33}}{dt} = -\frac{1}{3}c''_{33}[w(\nu'_{33},1,0;t) + 2w(\nu'_{33},1,\pm1;t)] + c'_{32}w(\nu''_{32},0,0;t) + \frac{2}{3}c''_{32}[w(\nu''_{32},1,0;t) + 2w(\nu''_{32},1,\pm1;t)], \quad \text{(B22)}$$

$$\frac{dc_{34}}{dt} = c_{33}w(\nu_{33},0,0;t) + \frac{1}{3}c''_{33}[w(\nu'_{33},1,0;t) + 2w(\nu'_{33},1,\pm1;t)] - 2c_{34}w(\nu_{34},0,0;t). \quad \text{(B23)}$$

APPENDIX C: PARAMETERS FOR KRYPTON AND XENON

Here the values of I_p, ν, $C^2_{\nu l}$, and B_{lm} are given for the two ionization cascades in krypton described by Eqs. (B6)–(B14) and Eqs. (B15)–(B23) and for the xenon case, that can be simulated using the same set of rate equations (B1)–(B5), changing the respective ionic state populations and their associated parameters.

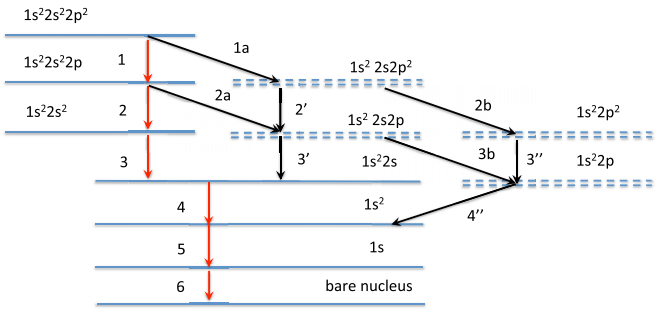

FIG. 9. Same as on Fig. 8 but for the initial ground state $1s^22s^22p^2$. See the text for details about the numeration of transitions and their parameters.

TABLE II. Parameters for the second ionization cascade of Kr (see text and Fig. 9 for more details).

Transition no.	z	I_p (eV)	ν	C^2	l	m	B_{lm}
1	31	3 584	1.910	0.325	1	0	3
1	31	3 584	1.910	0.325	1	±1	3/2
1a	31	3 671	1.887	1.048	0	0	1
2	32	3 752	1.927	0.327	1	0	3
2	32	3 752	1.927	0.327	1	±1	3/2
2a	32	3 819	1.910	1.039	0	0	1
2′	32	3 732	1.932	0.327	1	0	3
2′	32	3 732	1.932	0.327	1	±1	3/2
2b	32	3 841	1.904	1.041	0	0	1
3	33	3 971	1.931	1.030	0	0	1
3′	33	3 904	1.949	0.329	1	0	3
3′	33	3 904	1.949	0.329	1	±1	3/2
3b	33	3 975	1.930	1.031	0	0	1
3″	33	3 865	1.958	0.330	1	0	3
3″	33	3 865	1.958	0.330	1	±1	3/2
4	34	4 109	1.956	1.020	0	0	1
4″	33	4 038	1.973	0.331	1	0	3
4″	33	4 038	1.973	0.331	1	±1	3/2
5	35	17 296	0.981	0.990	0	0	1
6	36	17 936	0.991	0.995	0	0	1

TABLE III. Parameters for Xe.

Ionic state	e configuration	I_p (eV)	ν	C^2	l	m	B_{lm}
Xe^{50+}	$1s^2 2s^2$	9 607	1.919	1.035	0	0	1
Xe^{51+}	$1s^2 2s$	9 812	1.936	1.028	0	0	1
Xe^{52+}	$1s^2$	40 272	0.974	0.986	0	0	1
Xe^{53+}	$1s$	41 300	0.962	0.979	0	0	1

The first case of Kr corresponds to ionization of the outermost orbitals (red arrows on Fig. 8) and starts from the $1s^2 2s^2 2p^6$ state of Kr^{26+}. The parameters of the first ionization cascade are shown in Table I. The second one starts from the $1s^2 2s^2 2p^2$ state of Kr^{30+} and accounts for all pathways (shown by red and black arrows on Fig. 8). For this case one should take into account that several transitions may occur from or to a given state. These transitions are depicted and numbered in Fig. 9. The respective parameters are presented in Table II.

Finally, we run the same system of rate equations (B1)–(B5) for xenon starting from the ground-state configuration $1s^2 2s^2$ of the Xe^{50+} ion. The parameters are shown in Table III.

[1] C. Danson, D. Hillier, N. Hopps, and D. Neely, High Power Laser Sci. Eng. **3**, e3 (2015).

[2] M. D. Perry, D. Pennington, B. C. Stuart, G. Tietbohl, J. A. Britten, C. Brown, S. Herman, B. Golick, M. Kartz, J. Miller, H. T. Powell, M. Vergino, and V. Yanovsky, Opt. Lett. **24**, 160 (1999).

[3] S.-W. Bahk, P. Rousseau, T. A. Planchon, V. Chvykov, G. Kalintchenko, A. Maksimchuk, G. Mourou, and V. Yanovsky, Opt. Lett. **29**, 2837 (2004).

[4] V. Yanovsky, V. Chvykov, G. Kalinchenko, P. Rousseau, T. Planchon, T. Matsuoka, A. Maksimchuk, J. Nees, G. Cheriaux, G. Mourou, and K. Krushelnick, Opt. Express **16**, 2109 (2008).

[5] J-P. Chambaret, O. Chekhlov, G. Cheriaux *et al.*, Proc. of SPIE **7721**, 77211D (2010).

[6] A. V. Bashinov, A. A. Gonoskov, A. V. Kim, G. Mourou, and A. M. Sergeev, Eur. Phys. J. Spec. Top. **223**, 1105 (2014).

[7] E. Cartlidge, Science **359**, 382 (2018).

[8] A. S. Pirozhkov, Y. Fukuda, M. Nishiuchi, H. Kiriyama, A. Sagisaka, K. Ogura, M. Mori, M. Kishimoto, H. Sakaki, N. P. Dover, K. Kondo, N. Nakanii, K. Huang, M. Kanasaki, K. Kondo, and M. Kando, Opt. Express **25**, 20486 (2017).

[9] Z. Guo, L. Yu, J. Wang, C. Wang, Y. Liu, Z. Gan, W. Li, Y. Leng, X. Liang, and R. Li, Opt. Express **26**, 26776 (2017).

[10] S. Weber *et al.*, Matter Radiat. Extremes **2**, 149 (2017).

[11] G. A. Mourou, T. Tajima, and S. V. Bulanov, Rev. Mod. Phys. **78**, 309 (2006).

[12] A. Di Piazza, C. Müller, K. Z. Hatsagortsyan, and C. H. Keitel, Rev. Mod. Phys. **84**, 1177 (2012).

[13] N. B. Narozhny and A. M. Fedotov, Contemp. Phys. **56**, 249 (2015).

[14] U. Mohideen, M. H. Sher, H. W. K. Tom, G. D. Aumiller, O. R. Wood, R. R. Freeman, J. Bokor, and P. H. Bucksbaum, Phys. Rev. Lett. **71**, 509 (1993).

[15] G. G. Paulus, W. Nicklich, H. Xu, P. Lambropoulos, and H. Walther, Phys. Rev. Lett. **72**, 2851 (1994).

[16] K. Zrost, A. Rudenko, Th. Ergler, B. Feuerstein, V. L. B. de Jesus, C. D. Schröter, R. Moshammer, and J. Ullrich, J. Phys. B **39**, S371 (2006).

[17] M. Kübel, M. Arbeiter, C. Burger, N. G. Kling, T. Pischke, R. Moshammer, T. Fennel, M. F. Kling, and B. Bergues, J. Phys. B **51**, 134007 (2018).

[18] D. N. Fittinghoff, P. R. Bolton, B. Chang, and K. C. Kulander, Phys. Rev. Lett. **69**, 2642 (1992).

[19] A. Becker and F. H. M. Faisal, Phys. Rev. Lett. **84**, 3546 (2000).

[20] R. Kopold, W. Becker, H. Rottke, and W. Sandner, Phys. Rev. Lett. **85**, 3781 (2000).

[21] W. Becker, X. J. Liu, P. J. Ho, and J. H. Eberly, Rev. Mod. Phys. **84**, 1011 (2012).

[22] H. G. Hetzheim and C. H. Keitel, Phys. Rev. Lett. **102**, 083003 (2009).

[23] H. Bauke, H. G. Hetzheim, G. R. Mocken, M. Ruf, and C. H. Keitel, Phys. Rev. A **83**, 063414 (2011).

[24] E. A. Chowdhury, C. P. J. Barty, and B. C. Walker, Phys. Rev. A **63**, 042712 (2001).

[25] E. A. Chowdhury and B. C. Walker, J. Opt. Soc. Am. B **20**, 109 (2003).

[26] K. Yamakawa, Y. Akahane, Y. Fukuda, M. Aoyama, N. Inoue, and H. Ueda, Phys. Rev. A **68**, 065403 (2003).

[27] K. Yamakawa, Y. Akahane, Y. Fukuda, M. Aoyama, J. Ma, N. Inoue, H. Ueda, and H. Kiriyama, J. Mod. Opt. **50**, 2515 (2003).

[28] A. M. Perelomov, V. S. Popov, and M. V. Terentev, Zh. Eksp. Teor. Fiz. **50**, 1393 (1966) [Sov. Phys.—JETP **23**, 924 (1966)].

[29] A. M. Perelomov and V. S. Popov, Zh. Eksp. Teor. Fiz. **52**, 514 (1967) [Sov. Phys.—JETP **25**, 336 (1967)].

[30] M. V. Ammosov, N. B. Delone, and V. P. Krainov, Zh. Eksp. Teor. Fiz. **91**, 2008 (1986) [Sov. Phys.—JETP **64**, 1191 (1986)].
[31] V. S. Popov, Usp. Fiz. Nauk **174**, 921 (2004) [Phys. Usp. 47, 855 (2004)].
[32] S. V. Popruzhenko, J. Phys. B **47**, 204001 (2014).
[33] J. Fletcher and I. R. Cowling, J. Phys. B **6**, 258 (1973).
[34] L. P. Pitaevskii and E. M. Lifshitz, *Physical Kinetics* (Elsevier Science, Amsterdam, 2012).
[35] L. V. Keldysh, Zh. Eksp. Teor. Fiz. **47**, 1945 (1964) [Sov. Phys.—JETP **20**, 1307 (1965)].
[36] D. R. Hartree, Math. Proc. Cambridge Philos. Soc. **24**, 89 (1928).
[37] E. G. Gelfer, A. M. Fedotov, and S. Weber, Plasma Phys. Control. Fusion **60**, 064005 (2018).
[38] I. Yu. Kostyukov and A. A. Golovanov, Phys. Rev. A **98**, 043407 (2018).
[39] J. Strohaber, A. A. Kolomenskii, and H. A. Schuessler, J. Appl. Phys. **118**, 083107 (2015).
[40] E. B. Saloman, J. Phys. Chem. Ref. Data **36**, 215 (2007).
[41] W. H. Press, S. A. Teulkolsky, W. T. Vetterling, and B. P. Flannery, *Numerical Recipes in Fortran 90: Volume 2* (Cambridge University Press, Cambridge, UK, 1996).
[42] E. B. Saloman, J. Phys. Chem. Ref. Data **39**, 033101 (2010).
[43] E. B. Saloman, J. Phys. Chem. Ref. Data **33**, 765 (2004).